The active oxygen species promoted catalytic oxidation of 5-hydroxymethyl-2-furfural on facet-specific Pt nanocrystals

Yaqi Liu[†,‡,⊥], Hong-Yan Ma[§,∥,⊥], Da Lei[‡], Lan-Lan Lou[‡], Shuangxi Liu[‡], Wuzong Zhou[#], Gui-Chang Wang[∥,*], Kai Yu[†,*]

[†] MOE Key Laboratory of Pollution Processes and Environmental Criteria, Tianjin Key Laboratory of Environmental Technology for Complex Transmedia Pollution, College of Environmental Science and Engineering, Nankai University, Tianjin 300350, P. R. China

[‡] Institute of New Catalytic Materials Science and MOE Key Laboratory of Advanced Energy Materials Chemistry, School of Materials Science and Engineering, National Institute of Advanced Materials, Nankai University, Tianjin 300350, P. R. China

[§] RenAi college of Tianjin University, Tianjin 301636, P. R. China

[∥] MOE Key Laboratory of Advanced Energy Materials Chemistry, Tianjin key Lab and Molecule-based Material Chemistry, College of Chemistry, Nankai University, Tianjin 300071, P. R. China

[#] School of Chemistry, University of St Andrews, St Andrews, Fife KY16 9ST, United Kingdom

ABSTRACT: The aerobic oxidation of alcohols and aldehydes over noble metal catalysts is a critical reaction for the catalytic conversion of carbohydrates into value-added chemicals from biomass. However, to fully understand the reaction mechanism, in particular the role of O_2 and the generated active oxygen species in these reactions is still a challenging target. In the present work, the sub-10 nm Pt nanocrystals with cubic (Pt-NCs), octahedral (Pt-NOs) and spherical (Pt-NSs) morphologies were synthesized and used as catalysts in aerobic oxidation of HMF. Through experimental and computational investigations, the facet-dependent O_2 conversion pathway and catalytic oxidation performance were discussed. The molecular O_2 tends to be dissociated to generate •OH on Pt(100) surface, but prefers to be reduced to $•O_2^-$ on Pt(111) surface. Moreover, Pt-NCs enclosed by the {100} facets exhibited significantly enhanced catalytic activity than Pt-NOs enclosed by the {111} facets and Pt-NSs, in particular for alcohol oxidation step. Based on the experimental data and density functional theory (DFT) calculations, an active oxygen species promoted dehydrogenation mechanism for aerobic oxidation of HMF was proposed. The dehydrogenation of alcohol group is more favourable on the Pt(100) surface with an assistance of •OH, which are the dominant active oxygen species on the Pt(100) surface. We anticipate that this work would provide a new insight into the role of active oxygen species in aerobic oxidation of alcohols and aldehydes over noble metal catalysts.

KEYWORDS: *Pt nanocrystals; active oxygen species; aerobic oxidation of HMF; DFT calculations; facet-dependent performance.*

1. INTRODUCTION

Catalytic oxidation as a key reaction in current chemical industry has received much attention due to its significant role in the development of value-added chemicals from biomass.[1,2] In particular, the aerobic oxidation of alcohols and aldehydes is considered as a critical process for the catalytic conversion of carbohydrates into various organic acids and furan chemicals.[3,4] However, because of the complicated reaction system and multiple reaction pathway, to fully understand the reaction mechanism of liquid-phase selective aerobic oxidation of alcohols and aldehydes is still a challenging target.

5-Hydroxymethyl-2-furfural (HMF), as an important biomass platform chemical,[5] can act as a versatile chemical intermediate to produce various high value-added products.[6-8] In the last decade, a series of heterogeneous catalysts have been reported for the selective oxidation of HMF, such as noble metal nanocatalysts,[9,10] transition metal oxides,[11,12] photocatalysts[13,14] and enzyme.[15] Among them, noble metal nanocatalysts exhibited desirable activity and product selectivity under mild conditions, including ambient O_2 pressure, moderate alkalinity, and aqueous solution as reaction medium,[16,17] which has, accordingly, received more attention. In addition, the reaction from HMF to its final oxidation product, 2,5-furandicarboxylic acid (FDCA), involves one alcohol oxidation step and two aldehyde oxidation steps (as shown in Scheme S1). Therefore, the aerobic oxidation of HMF towards FDCA is regarded as an ideal model reaction to investigate the reaction mechanism of liquid-phase selective oxidation of alcohols and aldehydes on noble metal catalysts.

Many researches[18-21] have attempted to clarify the reaction mechanism of noble-metal catalyzed aerobic oxidation of HMF. Davis et al.[18] studied this reaction at high pH (2.0 mol/L NaOH) over supported Pt and Au catalysts through ^{18}O isotope labeling experiments, proving that H_2O is the source of oxygen atoms during the oxidation of HMF. Accordingly, the dehydrogenation mechanism of HMF on noble metal catalysts was proposed after combining the density functional theory (DFT) calculations.[22] In this mechanism, after excluding dissociation of O_2

under such a high-pH condition, the molecular O_2 was considered to play an indirect role during HMF oxidation by removing electrons from the metal surface,[22,23] and the dehydrogenation reaction was believed to proceed with the assistance of adsorbed hydroxide ions from the alkaline aqueous solution. Ardemani et al.[19] also reported that the basicity of reaction solution played a critical role in this reaction. With an increasing basicity, the reaction rates of aldehyde oxidation steps were enhanced obviously, but that for alcohol oxidation step changed quite mildly. Therefore, under commonly used low-moderate pH conditions, the reaction mechanism for aerobic oxidation of HMF on noble metal catalysts would be different.

It has been reported, through experimental and computational investigations, that noble metals exhibited very different catalytic behaviors in activation of O_2.[24] For instance, dissociation of O_2 was difficult to take place on the Au(111) and Ag(111) surfaces, but was favourable on the Pt(111) and Pd(111) surfaces. Such different catalytic behaviors for O_2 activation were found to be dependent on the metal composition,[25] exposed facet,[26] and solution pH value.[27] Taking into account of the multiple conversion pathways of O_2 on different noble metal catalysts, the roles of molecular O_2 and generated active oxygen species via O_2 activation in aerobic oxidation of HMF still need to be investigated in depth.

On the other hand, different types of noble metal catalysts, such as Pt, Pd, Au, Ru, Ag, exhibited variable selectivity for aerobic oxidation of HMF. For example, compared with Pt and Pd, Au exhibited higher activity for aldehyde oxidation step but lower activity for alcohol oxidation step under an alkaline condition.[21] Ru is inclined to oxidize the alcohol group of HMF instead of the aldehyde group, resulting in a formation of 2,5-diformylfuran (DFF) as an intermediate product, rather than 5-hydroxymethyl-2-furancarboxylic acid (HMFCA).[28] Recently, our group reported the facet-dependent performance of Pd nanocrystals in aerobic oxidation of HMF, and found that Pd(111) facets were more favorable for the alcohol oxidation step as compared with Pd(100) facets.[29] However, till now, our understanding on the structure-function relationship of noble metal nanocatalysts in complicated liquid-phase selective oxidation of alcohols and aldehydes is still insufficient.

In the present work, the sub-10 nm Pt nanocrystals with cubic, octahedral and spherical morphologies were synthesized by polyol alcohol methods and used as catalysts for the aerobic oxidation of HMF. The different catalytic behaviors of these Pt nanocrystals with specific facets in O_2 activation and HMF oxidation are detailedly investigated. Through the experimental and computational investigations, an active oxygen species promoted dehydrogenation mechanism for aerobic oxidation of HMF is proposed. We believe this work will provide some new insights into the mechanism of liquid-phase aerobic oxidation of alcohols and aldehydes over noble metal catalysts.

2. Experimental

2.1 Materials. All of the chemicals were of analytical grade and used as received without further purification. HMF (97%) and FDCA (98%) were purchased from Heowns Biochemical Technology Co., Ltd. HMFCA (98%) and 5-formyl-2-furancarboxylic acid (FFCA, 98%) were obtained from Matrix Scientific and Toronto Research Chemicals Inc., respectively. DFF (98%) was supplied by Sun Chemical Technology Co., Ltd. Chloroplatinic acid hexahydrate ($H_2PtCl_6 \cdot 6H_2O$), nitric acid (HNO_3, 68%), silver nitrate ($AgNO_3$, 99+%), ethylene glycol, phosphoric acid (H_3PO_4) and commercial 5 wt% Pt/C were purchased from Aladdin. Polyvinylpyrrolidone (PVP, MW~55000), absolute ethanol and hexane were obtained from Sales Chemistry Research Institute. 5,5-Dimethyl-1-pyroline N-oxide (DMPO) was purchased from Meryer (Shanghai) Chemical Technology Co., Ltd.

2.2 Synthesis of single-crystalline Pt nanocrystals. The Pt nanocrystals were prepared using a polyol alcohol method according to the literature.[30] In a typical experiment, ethylene glycol (3.0 mL) was heated to reflux for 5 min in a 160 ºC oil bath. Then, the solutions of $AgNO_3$ (0.5 mL, 0.002 mol/L), PVP (93.8 μL, 0.375 mol/L), and $H_2PtCl_6 \cdot 6H_2O$ (46.9 μL, 0.0625 mol/L) in ethylene glycol were sequentially added dropwise into the boiling ethylene glycol within 16 min. The resulting solution was heated at 160 ºC for 10 min until the color of the solution became dark-brown. After cooling to room temperature, the reaction solution was centrifuged at 8000 rpm for 15 min. The supernatant was collected and added into triple volume of acetone, followed by centrifuging at 5000 rpm for 5 min. The precipitate was re-dispersed in 3.0 mL of ethanol with sonication for 15 min before adding 9.0 mL of hexane, and the obtained mixture was centrifuged at 5000 rpm for 5 min. The Pt nanocubes (Pt-NCs) was dried in vacuum and then re-dispersed in deionized water for further use. For Pt nanooctahedrons (Pt-NOs) and nanospheres (Pt-NSs), the synthesis procedure was similar to that of Pt-NCs, but the concentrations of $AgNO_3$ solution were changed to 0.06 mol/L and 0.04 mol/L, respectively. In addition, the refluxing time of Pt-NSs was 6 h instead of 10 min. The concentrations of synthesized Pt nanocrystal colloidal dispersions were detected by inductively coupled atomic emission spectrometry (ICP-AES) before being used.

2.3 Specimen Characterization. Transmission electron microscopy (TEM) analysis of single-crystalline Pt nanocrystals were carried out on an FEI Tecnai G2 F20 instrument. The surface chemical compositions of samples were examined using X-ray photoelectron spectroscopy (XPS) on Axis Ultra DLD photoelectron spectrometer. ICP-AES characterization of the samples was performed on a Thermo Fisher Scientific Inc., IRIS Intrepid II XSP instrument. The electron paramagnetic resonance (EPR) signals of spin-trapped radicals were recorded on a Bruker EMX-6/1 spectrometer to detect the active oxygen species in the reaction system. In a typical EPR detection, Pt nanocrystals (0.004 mmol) were dispersed in 10 mL of deionized water, and then 100 μL of DMPO solution (100 mmol/L) was added in this mixture. The resulting solution was heated at 40 ºC for 10 min bubbled with O_2 (50 mL/min) and sampled for EPR detection. The reaction results of aerobic oxidation of HMF were analyzed using an Agilent 1200 series high-performance liquid chromatography (HPLC) equipped with a Sepax Carbomix H-NP10:8% column (column oven at 65 ºC) and a UV-Vis detector operating at 271 nm. 1 mmol/L H_3PO_4 aqueous solution was used as mobile phase at a flow rate of 0.6 mL/min.

2.4 HMF oxidation reaction. The aerobic oxidation of HMF was carried out in a 25.0 mL three neck flask equipped with magnetic stirring and a heating oil bath at 100 ºC. HMF (0.2 mmol), $NaHCO_3$ (0.8 mmol) and desired amount of Pt nanocrystal catalysts (Pt/HMF molar ratio=1:50) were suspended in 10 mL of deionized water bubbled with O_2 flow (75 mL/min). After a certain reaction time, 50 μL of reaction mixture was

taken out, diluted with 5 mL of deionized water, and syringe-filtered using 0.2 μm PTFE membrane for HPLC test.

2.5 Computational methods. The computations of the reaction mechanism over Pt nanocrystals were performance using the Vienna ab initio simulation package (VASP)[31-33] by the self-consistent periodical density functional theory (DFT) calculations with the projected augmented wave (PAW)[34] pseudopotentials. All electronic structures were calculated using the Perdew−Burke−Ernzerhof (PBE)[35] form of the generalized gradient approximation (GGA) expanded in a plane wave basis with a kinetic cutoff energy of 400 eV. The climbing image general nudged elastic band (CI-NEB)[36] method was employed to locate the transition states (TSs). Spin polarization was included in the calculations.

The calculated lattice constant of bulk Pt is 3.977 Å, very close to the experimental value of 3.912 Å.[37] The Pt(111) and Pt(100) facets were modeled by the p(4 × 4) unit cell of four layers, in which the uppermost two layers and the adsorbed species were relaxed during the optimization processes. A vacuum space of 2.0 nm was applied in the case of the spurious interactions normal to the surface. A 3 × 3 × 1 Monkhorst−Pack k-point mesh[38] was used in the surface Brillouin zone. The activation energies (E_a), and reaction energies (ΔE) were calculated by the following three formulas: $E_a = E_{TS} - E_{IS}$, and $\Delta E = E_{FS} - E_{IS}$, respectively. Here, E_{TS}, E_{IS}, and E_{FS} denote the calculated energies of the transition state (TS), initial state (IS), and final state (FS), respectively.

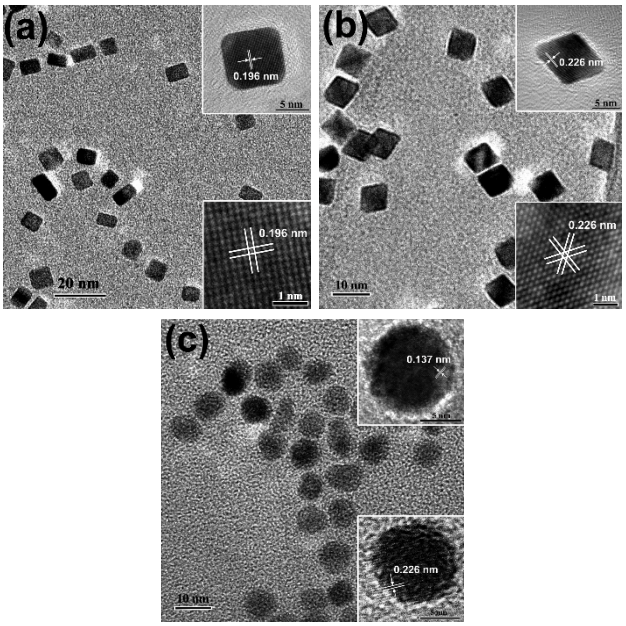

Figure 1. TEM and HRTEM images of (a) Pt-NCs, (b) Pt-NOs and (c) Pt-NSs samples. The insets in (a-c) are the HRTEM images of Pt nanocrystals. The measured *d*-spacings of 0.196 nm, 0.226 nm, and 0.137 nm correspond to the {200}, {111} and {220} planes of Pt, respectively.

RESULTS AND DISCUSSION

3.1 Characterization of single-crystalline Pt nanocrystals. Figure 1 describes the representative TEM and HRTEM images of Pt-NCs, Pt-NOs and Pt-NSs samples. It can be clearly observed that all the samples are highly monodisperse with well-defined morphologies. The lattice spacing of 0.196 nm, observed in the insets of Figure 1a, corresponds to the interplanar distance of the {200} planes of the face-centred cubic (fcc) structure of Pt with a = 0.392 nm, demonstrating that the surface of Pt-NCs particles is terminated at the {100} planes.[39] The measured interplanar distance of Pt-NOs in the insets of Figure 1b is 0.226 nm, corresponding to the lattice spacing of the {111} planes of the fcc structure of Pt. The representative images (Figure 1c) of the Pt spherical crystals demonstrate the coexistence of a variety of planes, including {100} and {110} planes, on the surface of Pt-NSs, which is consistent with the reported work.[40] The corresponding low magnification TEM images showing many particles with the particle size distributions are presented in Figure S1. A narrow size distribution of Pt nanocrystals can be observed, which was measured for more than 200 randomly chosen particles. The mean particle sizes of Pt-NCs, Pt-NOs and Pt-NSs are 7.2 nm, 9.2 nm and 8.7 nm, respectively. Although these Pt nanocrystals have different particle sizes, the calculated percentages of surface atoms in Pt-NCs and Pt-NOs are very similar (about 15%) (Table S1), allowing a reasonable comparison of catalytic activity over these Pt nanocrystals.

The obtained Pt nanocrystals were characterized by XPS to determine their chemical compositions and valence states. The wide range XPS spectra of Pt nanocrystals (Figure S2) indicated the existence of Pt, Ag, C, N, O elements in these samples. The C, N and O elements come from PVP, and the trace amount of Ag can be ascribed to the residual Ag species, which was used to control the shape of Pt nanocrystals. Figure 2 shows the high-resolution XPS spectra in Pt 4f and Ag 3d regions of the as-prepared Pt-NCs, Pt-NOs and Pt-NSs samples. As shown in Figure 2a, the Pt 4f signal can be deconvoluted into two components with binding energies centered at about 70.9 eV and 74.3 eV, which are ascribed to $4f_{7/2}$ and $4f_{5/2}$ states of Pt^0, respectively. The relative weaker peaks located at about 72.2 eV and 75.6 eV can be attributed to the Pt^{2+} species, with a concentration lower than 19%. The presence of Pt^{2+} species can be attributed to the exposure of these Pt nanocrystals to O_2.[41]

The Ag 3d XPS spectra of these Pt nanocrystals are shown in Figure 2b. The weak intensities of these XPS peaks in Ag 3d regions of the Pt nanocrystals indicated that a small amount of residual Ag species on the surface of Pt nanocrystals, which was also found by Grass et al.[42] The amount of residual Ag in the obtained Pt nanocrystals was detected by ICP-AES and the results are shown in Table S2. It can be seen that 5.67% of Ag residue was detected on Pt-NOs, which is obviously higher than that on Pt-NCs (0.90%) and Pt-NSs (2.85%) due to the obviously higher dosage of $AgNO_3$ during the synthesis of Pt-NOs. In order to eliminate the probable influence of residual Ag on the catalytic performance, the obtained Pt nanocrystals were treated by HNO_3 solution to remove the residual Ag according to the reported method.[42] Through the detection of ICP-AES, it can be found that after etching with HNO_3 solution, the residual amount of Ag on Pt-NOs and Pt-NSs notably decreased to 0.90% and 0.82%, respectively. The Ag 3d XPS spectra of Pt nanocrystals after etching treatment are shown in Figure S3. It can

be observed that the Ag 3d XPS peaks of these samples are negligible, indicating that the Ag residues were efficiently removed by etching treatment with HNO_3 solution. The small amount of remained Ag residues on Pt-NCs and Pt-NOs after etching treatment (Table S2) should exist in the interior of Pt nanocrystals, which will hardly influence the catalytic performance of Pt nanocrystals. The TEM characterization of Pt nanocrystals after etching treatment indicated that the morphologies of these Pt nanocrystals were well maintained after etching treatment (Figure S4). The negligible influence of residual Ag species on catalytic performance of these Pt nanocrystals will be discussed in section 3.3.

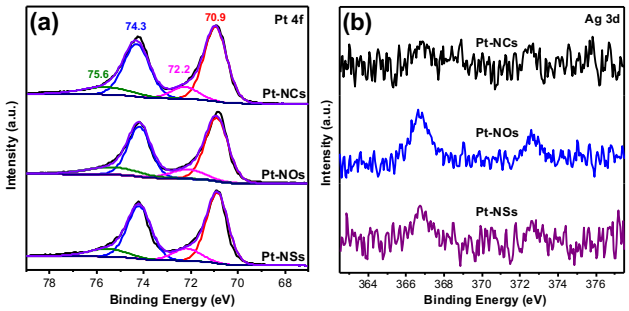

Figure 2. High-resolution XPS spectra of Pt nanocrystals in the (a) Pt 4f and (b) Ag 3d regions.

3.2 The different conversion pathway of O_2 on Pt nanocrystals. In order to study the different conversion pathway of O_2 on Pt nanocrystals with specific facet exposed, the EPR characterizations of Pt-NCs and Pt-NOs were performed to detect the active oxygen species, including hydroxyl radical (•OH) and superoxide radical ($•O_2^-$), which are the products of O_2 activation through dissociation and reduction reaction, respectively. As shown in Figure 3a, four characteristic peaks with an intensity ratio of 1:2:2:1, corresponding to the EPR signals of DMPO-•OH adducts, were clearly observed on Pt-NCs, while no obvious EPR signal can be detected on Pt-NOs. On the contrary, as described in Figure 3b, four characteristic peaks with an intensity ratio of 1:1:1:1 attributed to the EPR signals of DMPO-$•O_2^-$ adducts can be detected over Pt-NOs, but the relevant peaks cannot be observed on Pt-NCs. The different active oxide radicals generated on Pt-NCs and Pt-NOs indicate the facet-dependent conversion pathway of O_2 on Pt nanocrystals. The O_2 molecules tend to be dissociated to O atoms on the {100} facets of Pt nanocrystals and then react with adsorbed H_2O to form •OH, as described in eqs(1) and (2). While, the O_2 molecules adsorbed on the {111} facets of Pt nanocrystals prefer to be reduced to $•O_2^-$, as described in eq(3). In aqueous solution, the generated $•O_2^-$ will be further reduced and react with H_2O to generated OOH^- and OH^- followed by eq(4).

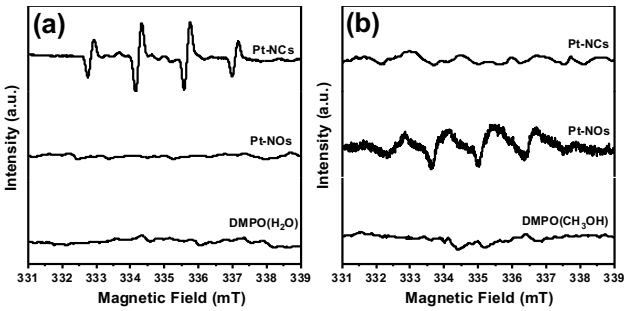

Figure 3. EPR spectra of radical adducts with DMPO over Pt-NCs and Pt-NOs after O_2 bubbling (50 mL/min) for 10 min at 40 ºC in (a) aqueous and (b) methanol dispersions.

$$O_2 \rightarrow O^* + O^* \quad (1)$$

$$O^* + H_2O \rightarrow •OH + •OH \quad (2)$$

$$O_2 + e \rightarrow •O_2^- \quad (3)$$

$$•O_2^- + H_2O + e \rightarrow OOH^- + OH^- \quad (4)$$

In order to further investigate the different conversion pathway of O_2 on Pt-NOs and Pt-NCs, DFT calculations were carried out for the adsorption of O_2 and the reaction between O_2 and H_2O on the surfaces of Pt(100) and Pt(111). Figure S5 shows the geometries and the adsorption energies (E_{ads}) for O_2 on Pt(100) and Pt(111). It can be observed that the adsorbed O_2 lies almost parallel to the surface of Pt at the lowest-energy adsorption configurations. The O-O distances (d_{O-O}) of adsorbed O_2, which are 1.36 Å on Pt (100) and 1.37 Å on Pt (111), are obviously larger than that of free molecular O_2 (1.23 Å), indicating the activation of O_2 on Pt surface. The calculated adsorption energy of O_2 on Pt(100) is obviously lower than that on Pt(111), suggesting the stronger adsorption ability of Pt(100) for O_2 molecules, which should be beneficial to the dissociation of O_2 molecule[24] and the subsequent reaction between O_2 and H_2O.

The reaction between O_2 and H_2O on Pt(100) and Pt(111) are calculated, and the energy profiles and optimized TSs are shown in Figure 4. The reaction on Pt(111) was found to be a two-step mechanism. Firstly, the O-H bond was broken, and then the O-O bond was broken. The step of $H_2O + O_2 \rightarrow OH + OOH$ has a barrier of 0.52 eV via TS1 ($d_{O-H/O-H}$ = 1.04/1.53 Å, Figure 4), and it is endothermic by 0.50 eV. After that, the formed OOH reacted with H_2O to form H_2O_2 and OH via TS2, and the energy barrier of this step was calculated to be 0.95 eV with the reaction energy of +0.93 eV. At last, the formed H_2O_2 underwent O-O bond scission via TS3 (d_{O-O} = 1.77 Å, Figure 4) to form 2OH species. The energy barrier of this step was found to be 0.45 eV, and it is exothermic by 1.59 eV. The reaction process was considered as the following steps, $O_2 + 2H_2O \rightarrow OOH + OH + H_2O \rightarrow H_2O_2 + 2OH \rightarrow 4OH$.

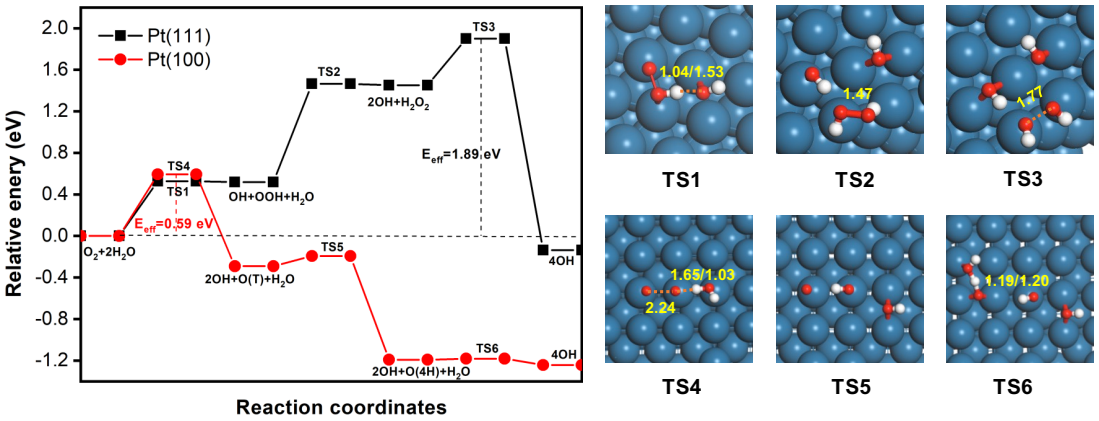

Figure 4. Energy profiles and optimized TSs of the reaction between H_2O and O_2 on Pt(100) and Pt(111). O(T) means oxygen atom binds to atop site of Pt atom and O(4H) means oxygen atom binds to four-fold hollow site. The Pt, O, and H atoms are colored blue, red and white, respectively. The distances (angstrom-unit) between adatoms are marked on TSs.

On Pt(100), however, the relevant reaction was found to be a one-step mechanism. Firstly, O-O bond and O-H bond were simultaneously broken (*i.e*, a cooperative mechanism), and the products were two adsorbed OH species and one oxygen atom bound to atop site of Pt [denoted as 2OH + O(T)]. The reaction energy of $H_2O + O_2 \rightarrow 2OH + O(T)$ was calculated to be exothermic by -0.30 eV, and the energy barrier was 0.59 eV through TS4 ($d_{O\text{-}O}$ = 2.24 Å, $d_{O\text{-}H/H\text{-}O}$ = 1.65/1.03 Å, Figure 4). After the formation of 2OH + O(T) state, the oxygen species migrated from the atop site to the fcc site and released the energy of 0.90 eV. Finally, the formed oxygen species reacted with H_2O to form 2OH through TS6 ($d_{O\text{-}H/O\text{-}H}$ = 1.19/1.20 Å, Figure 4), which is a barrierless elemental step. The formation process of OH species on Pt(100) can be expressed as $O_2 + 2H_2O \rightarrow 2OH + O(T) + H_2O \rightarrow 2OH + O(4H) + H_2O \rightarrow 4OH$, which is different from the situation of Pt(111).

For the whole reaction process of $O_2+2H_2O \rightarrow 4OH$ as discussed above, the apparent activation energy on the Pt(111) surface is 1.89 eV, while it is only 0.59 eV on Pt(100). Moreover, it should be noted that the reaction on Pt(100) is more exothermic compared with that on Pt(111), namely Pt(100) surfaces are both thermodynamics and kinetics favorable for OH formation. Thus, the coverage of OH species is higher on Pt(100), which should be conducive to further dehydrogenation reaction.

The reason why Pt(100) facet is more active than Pt(111) is that the atoms on (100) planes are more roughly arranged and the metal coordination number is relatively low. Pt atom at the (111) surface coordinated with 9 Pt atoms (6 in the same plane and 3 underneath). But Pt atom at the (100) surface is 8 coordinated with other Pt atoms (4 in the same plane and 4 underneath). The relatively lower coordination number of Pt atoms on the (100) surface is favorable for the adsorption of molecular O_2 and would be beneficial to the dissociation reaction of O_2.

3.3 HMF oxidation over Pt nanocrystals. The obtained Pt nanocrystals with specific facet exposed were evaluated in the aerobic oxidation of HMF. Figure 5 shows the reaction profiles over these Pt nanocatalysts. No DFF was detected from these reaction solutions because of the alkaline reaction condition. It can be found that Pt-NCs enclosed by the {100} facets exhibited the highest catalytic activity. After 10 h reaction, full conversion of HMF and 95.1% yield of FDCA were achieved. While for Pt-NOs, only 85.1% conversion of HMF and 24.9% yield of FDCA were obtained in the same reaction time. Pt-NSs exhibited the moderate catalytic activity (full conversion of HMF and 46.5% yield of FDCA) among these Pt nanocatalysts. The used Pt nanocrystals were characterized by TEM (Figure S6) and XPS (Figure S7). No obvious changes can be observed in morphology and chemical state of these Pt nanocrystals after aerobic oxidation reactions.

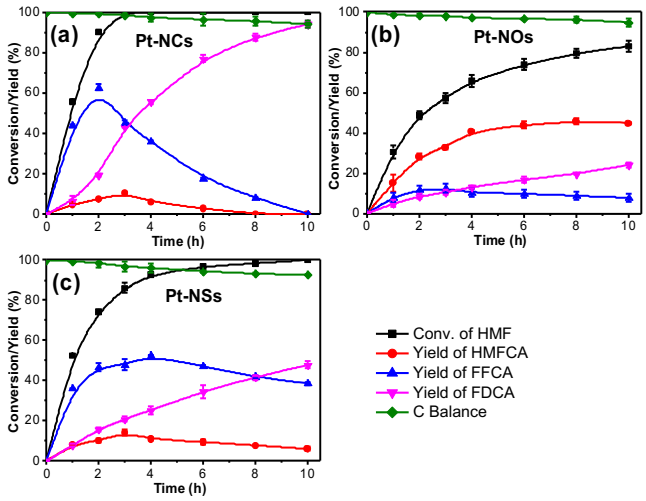

Figure 5. Reaction profiles for HMF oxidation over (a) Pt-NCs, (b) Pt-NOs, and (c) Pt-NSs at ambient pressure. Reaction conditions: n_{HMF}/n_{Pt}(mol/mol) = 50, n_{NaHCO3}/n_{HMF}(mol/mol) = 4, 100 ºC, O_2 bubbling (75 mL/min).

In order to directly compare the catalytic performance of these Pt nanocrystal catalysts to the ever reported catalysts, the turnover frequency (TOF) values were calculated from the results at 5 min reaction (Figure 5) using the eq(5).[43] Pt dispersion, that is the surface atom percentage of Pd catalyst, was determined by geometrical configurations and average particle sizes (Table S1). The calculated TOF values of Pt-NCs and Pt-NOs were 6.53 min^{-1} and 3.06 min^{-1}, respectively. Compared with ever reported noble metal nanocatalysts, Pt-NCs exhibited

relatively high activity for aerobic oxidation of HMF under mild conditions.[43-46]

$$TOF(min^{-1}) = \frac{Conv_{HMF}(\%) \times (n_{HMF}/n_{Pt})}{time(min) \times Pt\ dispersion} \quad (5)$$

Interestingly, as shown in Figure 5, HMFCA is the major intermediate in the aerobic oxidation of HMF catalyzed by Pt-NOs, while FFCA is the main intermediate in the reactions over Pt-NCs and Pt-NSs, suggesting the obviously lower reaction efficiency from HMFCA to FFCA over Pt-NOs. In order to represent their catalytic performance directly, the kinetic parameters of each oxidation steps, including k_1 (HMF → HMFCA), k_2 (HMFCA → FFCA), and k_3 (FFCA → FDCA), over Pt-NCs and Pt-NOs were estimated according to the reported methods.[47,48] The adopted reaction kinetic model is described in Supporting Informations, and the calculated curve fitting results are described in Figure S8 based on the reaction results in Figure 5. The calculated reaction rate constants are listed in Table 1.

Table 1. Kinetic parameters estimated for the aerobic oxidation of HMF over Pt nanocrystals.

Catalyst	Rate constant (h^{-1})		
	k_1 (HMF→HMFCA)	k_2 (HMFCA→FFCA)	k_3 (FFCA→FDCA)
Pt-NCs	0.92	4.09	0.34
Pt-NOs	0.26	0.11	0.32

It can be found that the calculated rate constants of Pt-NCs are notably higher than those of Pt-NOs, in particular, the k_2 value of Pt-NCs is 37-fold higher than that of Pt-NOs, indicating the obviously enhanced catalytic performance of Pt-NCs in alcohol oxidation step. Moreover, it can be found that the rate-determining step in aerobic oxidation of HMF over Pt-NCs and Pt-NOs is different. The alcohol oxidation (HMFCA → FFCA) is the rate-determining step for Pt-NOs, but it is the fastest step for Pt-NCs. The second aldehyde oxidation (FFCA → FDCA) is the rate-determining step for Pt-NCs. In order to further confirm the different catalytic behaviors between Pt-NCs and Pt-NOs for the reaction from HMFCA to FFCA, an interrupt reaction experiment was carried out and the results are shown in Figure S9. A typical experiment of HMF oxidation over Pt-NOs was terminated after 6 h, and then the Pt-NOs catalyst was separated from the solution by centrifugation and the equivalent amount of Pt-NCs was added. The reaction was continued for another 6 h. It can be clearly seen from Figure S9, HMFCA was the major intermediate when Pt-NOs was used as catalyst, however, when Pt-NOs was replaced by Pt-NCs, HMFCA was rapidly converted and the yield of FDCA increased quickly, indicating the superior catalytic activity of Pt-NCs for the alcohol group oxidation.

In order to eliminate the influence of Ag residue on catalytic performance of Pt nanocrystals, the etching treated Pt-NCs, Pt-NOs and Pt-NSs catalysts were used as catalysts in the aerobic oxidation of HMF and the reaction results are shown in Figure S10. It can be seen that these etching treated Pt nanocrystals exhibited very similar catalytic activity compared with original samples (Figure 5), implying the negligible influence of Ag residue on Pt nanocrystals, and further indicating that the facet-dependent effect of these Pt nanocrystals is the key factor in this work.

3.4 DFT calculations for HMFCA dehydrogenation on Pt nanocrystals. As mentioned above, Pt nanocrystals exhibited facet-dependent catalytic activities in aerobic oxidation of HMF, in particular, for the alcohol oxidation step (HMFCA → FFCA). At the same time, these Pt nanocrystals showed very different conversion pathways of O_2, resulting in the surface coverage of different active oxygen species. Therefore, the influence of active oxygen species generated on Pt nanocrystals with specific facet exposed, including •OH and $•O_2^-$, on the dehydrogenation of HMFCA was urgent to be investigated. Through DFT calculations, the dehydrogenation steps of HMFCA* → HMFCA-H* + H* and HMFCA-H* → FFCA* + H* on Pt(100) and Pt(111) surfaces were studied. Since •OH prefers to be generated on Pt(100) surface and $•O_2^-$ is inclined to be formed on Pt(111) surface, the Pt(100) is pre-covered by OH* and the Pt(111) is pre-covered by O_2* in the present calculations. The results are shown in Figure 6. In addition, for comparison, the dehydrogenation steps of HMFCA on clean surfaces of Pt(100) and Pt(111) were also calculated and the results are shown in Figure S11.

On Pt(100), for the first step of O-H bond scission (HMFCA* + OH* → HMFCA-H* + H_2O*) with the assistance of OH*, its energy barrier was found to be 0.22 eV via TS7 ($d_{O\text{-}H/H\text{-}O}$ = 1.16/1.31 Å) and the reaction energy was -0.24 eV. For the second step of O-H bond scission (HMFCA-H*+OH*→FFCA*+H_2O*), the energy barrier was calculated to be 0.74 eV through TS8 ($d_{O\text{-}H/C\text{-}H}$ = 1.21/1.37 Å) with the reaction energy of -0.35 eV. However, it can be found from Figure S11, relatively lower barrier (0.47 eV) can be observed for the C-H bond scission process on clean Pt(100) surface. If the formed water by the first dehydrogenation step desorbed from the Pt(100), then a direct C-H bond scission process would be taken place through TS8' ($d_{C\text{-}H}$ = 1.48 Å). Therefore, the dehydrogenation reaction of HMFCA on OH* pre-covered Pt(100) includes an O-H bond scission under the assistance of OH* and a direct C-H bond scission, which is an exothermic process with the largest energy barrier of 0.47 eV.

However, for the first step of O-H bond scission on O_2* pre-covered Pt(111) surface, its energy barrier was found to be 0.54 eV through TS9 ($d_{O\text{-}H/H\text{-}O}$ = 1.04/1.66 Å) and the corresponding heat was exothermic by -0.87 eV. For the next C-H bond scission, the energy barrier through TS10 ($d_{O\text{-}H/C\text{-}H}$ = 1.32/1.32 Å) was found to be 0.84 eV, higher than that of the first O-H bond scission. Similarly with Pt(100) surface, relatively lower barrier (0.49 eV) can be observed for the C-H bond scission process on clean Pt(111) surface (Figure S11). Therefore, a direct C-H bond scission process would be taken place through TS10' ($d_{C\text{-}H}$ = 1.46 Å). The dehydrogenation reaction of HMFCA on O_2* pre-covered Pt(111) is an exothermic process with the largest energy barrier of 0.54 eV.

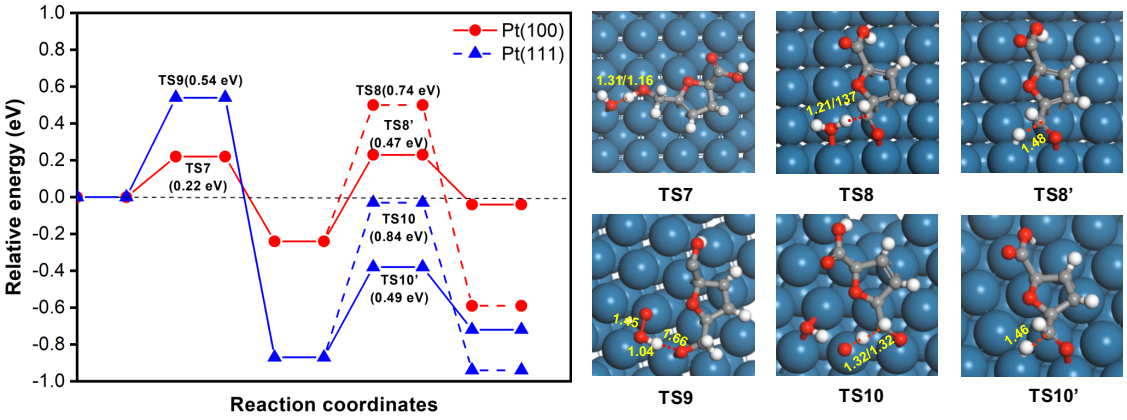

Figure 6. Energy profiles and optimized configurations of TSs for the O-H bond scission and C-H bond scission of HMFCA on active oxygen species pre-covered Pt(111) and Pt(100). The data in parentheses means the activation energy of related elemental step. The Pt, O, C and H atoms are colored blue, red, grey and white, respectively. The distances (angstrom-unit) between adatoms are marked on TSs.

It can be found from Figure S11, the first step of O-H bond scission has the relatively higher energy barriers (> 1.0 eV) for the dehydrogenation of HMFCA on clean surfaces of Pt(100) and Pt(111). The presence of active oxygen species on Pt(100) and Pt(111) surfaces can significantly decrease the energy barriers for the first step of O-H bond scission, resulting in the obviously promoted catalytic activity for the dehydrogenation reaction of HMFCA on active oxygen species pre-covered Pt(100) and Pt(111) surfaces. When comparing the DFT calculation results on active oxygen species pre-covered Pt(111) and Pt(100) surfaces, it can be found that OH* pre-covered Pt(100) surface is much more favorable for the formation of FFCA. The energy barrier of the first step of O-H bond scission is very low assisted by the active oxygen specie of OH*,[49-51] moreover, the energy barrier of the second C-H bond scission is also lower than that of O_2* pre-covered Pt(111) surface. Because of the low reaction barrier of O_2 dissociation on the surface of Pt(100) (Figure 4), more •OH would be generated, which has been proved by EPR characterization (Figure 3). Consequently, the Pt-NCs enclosed by {100} facets exhibited the highest catalytic activity for aerobic oxidation of HMF, in particular for the alcohol oxidation step.

3.5 The active oxygen species promoted catalytic performance of Pt nanocrystals. From experimental and computational investigations, the active oxygen species generated on noble metal catalysts should play a crucial role in promoting dehydrogenation of HMFCA. In ever reported mechanism for aerobic oxidation of HMF[18,22], the molecular O_2 was regarded to play an indirect role in the aerobic oxidation of HMF, the O_2 dissociation on noble metal catalysts was eliminated due to the high surface coverages of hydroxide ions at a high pH value (>14), and the hydroxide ions were considered as promoter for dehydrogenation of alcohol group. However, under commonly used low-moderate pH conditions, for example, $NaHCO_3$ or Na_2CO_3 as the soluble base, the O_2 dissociation should take place on the surface of catalysts, and the active oxygen species should be generated on the surface of noble metals. To prove this point, the EPR characterization of Pt-NCs under different pH values (from 7 to 10) was performed to investigate the generation of •OH. The detected results are shown in Figure 7. It can be found that with the increase of the pH value from 7 to 10, the characteristic EPR signals for DMPO-•OH adducts can be clearly observed for Pt-NCs sample, despite the intensity of the peaks decreased slightly. In this work, the initial pH value of the reaction solution is about 9 and the final pH value of the reaction solution is about 10. It indicates that the O_2 dissociation can take place on Pt-NCs under low-moderate pH conditions, and the •OH can be generated on the surface of Pt(100).

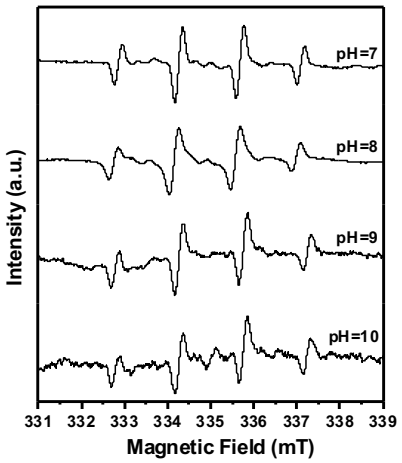

Figure 7. EPR spectra of radical adducts with DMPO over Pt-NCs after O_2 bubbling (50 mL/L) for 10 min at 40 ºC in aqueous dispersion with different pH values.

Based on the discussions above, an active oxygen species promoted dehydrogenation mechanism is proposed for aerobic oxidation of HMF on Pt nanocrystals with specific facets exposed as described in Figure 8. On the {100} facets of Pt nanocrystals, the molecular O_2 is dissociated to O atoms and reacts with H_2O to form •OH species, which can act as a promoter to the scission of O-H and C-H bonds of HMFCA, and accelerate the dehydrogenation reaction from HMFCA to FFCA. While, on the {111} facets of Pt nanocrystals, the molecular O_2 tends to be reduced to $•O_2^-$ and reacts with H_2O to form OOH^- and OH^- species. Although these adsorbed $•O_2^-$ species can also decrease the energy barriers of the dehydrogenation steps of HMFCA, the obviously higher energy barrier of O_2 and H_2O on

Pt(111) surface hindered the formation of active oxygen species. Thus, the dehydrogenation reaction from HMFCA to FFCA is inhibited to some extent on Pt-NOs.

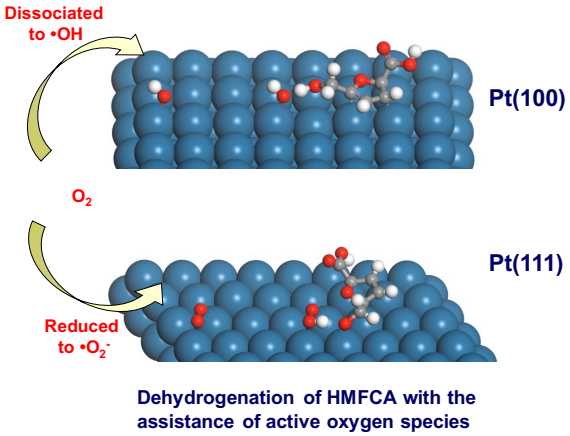

Figure 8. The proposed active oxygen species promoted dehydrogenation mechanism for alcohol oxidation step of HMF oxidation on the surfaces of Pt(100) and Pt(111).

Compared with ever reported mechanism, the proposed mechanism in this work put forward a possibility that the active oxygen species generated through O_2 activation directly take part in the dehydrogenation reaction of alcohols. In order to further confirm the promoting effect of active oxygen species for dehydrogenation of alcohols, the aerobic oxidations of HMFCA over Pt-NCs under base or base-free conditions were carried out, and the results for the first 1 h are shown in Figure S12. In this experiment, the initial activity was investigated because the subsequent aldehyde oxidation step (FFCA→FDCA) would be promoted under alkaline conditions, resulting in the acceleration of HMFCA oxidation. It can be clearly observed that, in particular for the first 15 minutes, the conversions of HMFCA over Pt-NCs are very similar under base-free or base conditions. It indicates that the hydroxide ions in alkaline solution might not be the promoter for dehydrogenation of alcohol group of HMFCA under low-moderate pH conditions, which provides an indirect experimental evidence for our proposed mechanism.

4. Conclusion

In the present work, an active oxygen species promoted reaction mechanism for aerobic oxidation of HMF was proposed by using Pt nanocrystals with specific facets exposed as catalysts. Through EPR characterization and DFT calculations, the different conversion pathways of O_2 on Pt nanocrystals were demonstrated. On Pt(100) surface, O_2 molecules tend to be dissociated to O atoms and react with H_2O to form •OH. While, on Pt(111) surface, O_2 molecules prefer to be reduced instead of being dissociated, resulting in the formation of $•O_2^-$ as determined by EPR characterization. The rougher atomic arrangement and relatively low coordination number of Pt atoms on (100) surface should be beneficial to the dissociation of O_2. The dehydrogenation reactions of HMFCA to FFCA on active oxygen species pre-covered Pt(100) and Pt(111) surfaces were studied by DFT calculations. It was found that the presence of active oxygen species can obviously decrease the energy barrier of the O-H bond scission of HMFCA. OH* pre-covered Pt(100) surface is more favorable for the dehydrogenation of HMFCA towards FFCA compared with O_2* pre-covered Pt(111) surface, which was also confirmed by the catalytic reaction results. Pt-NCs enclosed by the {100} facets exhibited significantly enhanced catalytic activity for aerobic oxidation of HMF compared with Pt-NOs enclosed by the {111} facets and Pt-NSs. In particular, for the alcohol oxidation step (HMFCA→FFCA), the calculated rate constant on Pt-NCs is significantly higher than that on Pt-NOs. We anticipate that this work may shed light on the further investigation of the mechanism of selective aerobic oxidation of alcohols and aldehydes over noble metal catalysts, and many other catalytic reaction systems where the active oxygen species are involved.

ASSOCIATED CONTENT

Supporting Information. Reaction pathway of HMF to FDCA, TEM images of Pt nanocrystals with particle size distributions, calculation for surface atom percentages of Pt nanocrystals, the molar ratio of Ag/Pt of Pt nanocrystals detected by ICP-AES, wide range XPS spectra of Pt nanocrystals, high-resolution Ag 3d XPS spectra and TEM images of Pt nanocrystals after etching treatment, the geometries and the adsorption energies for O_2 on Pt(100) and Pt(111), TEM images and XPS spectra (wide range and Pt 4f) of Pt nanocrystals after aerobic oxidation reactions, the reaction kinetic model for aerobic oxidation of HMF over Pt nanocrystals, reaction profile for an interrupt reaction experiment, reaction profiles for HMF oxidation over Pt nanocrystals after etching treatment, DFT calculations for dehydrogenation steps of HMFCA on clean Pt surfaces, reaction profiles for aerobic oxidation of HMFCA over Pt-NCs under base-free or base conditions. This material is available free of charge via the Internet at http://pubs.acs.org.

AUTHOR INFORMATION

Corresponding Author

* K.Y.: tel, +86-22-85358635; e-mail, kaiyu@nankai.edu.cn.
* G.W.: tel, +86-22-23503824; e-mail, wangguichang@nankai.edu.cn.

ORCID

Wuzong Zhou: 0000-0001-9752-7076
Guichang Wang: 0000-0001-8137-6007
Kai Yu: 0000-0001-7569-3276

Author Contributions

⊥These authors contributed equally.

Notes

The authors declare no competing financial interest.

ACKNOWLEDGMENT

This work was supported by Natural Science Foundation of Tianjin (Grant No. 17JCYBJC22600) and the Fundamental Research Funds for the Central Universities.

REFERENCES

(1) Davis, S. E.; Ide, M. S.; Davis, R. J. Selective Oxidation of Alcohols and Aldehydes over Supported Metal Nanoparticles. *Green Chem.* **2013**, *15*, 17−45.

(2) Guo, Z.; Liu, B.; Zhang, Q.; Deng, W.; Wang, Y.; Yang, Y. Recent Advances in Heterogeneous Selective Oxidation Catalysis for Sustainable Chemistry. *Chem. Soc. Rev.* **2014**, *43*, 3480−3524.

(3) Zhang, Z.; Huber, G. W. Catalytic Oxidation of Carbohydrates into Organic Acids and Furan Chemicals. *Chem. Soc. Rev.* **2018**, *47*, 1351−1390.

(4) Zhang, X.; Wilson, K.; Lee, A. F. Heterogeneously Catalyzed Hydrothermal Processing of C5–C6 Sugars. *Chem. Rev.* **2016**, *116*, 12328−12368.

(5) Werpy, T.; Petersen, G. Top Value Added Chemicals from Biomass Volume I—Results of Screening for Potential Candidates from Sugars and Synthesis Gas, Report PNNL-14808, Pacific Northwest National Laboratory, **2004**.

(6) Rosatella, A. A.; Simeonov, S. P.; Frade, R. F. M.; Afonso, C. A. M. 5-Hydroxymethylfurfural (HMF) as a Building Block Platform: Biological Properties, Synthesis and Synthetic Applications. *Green Chem.* **2011**, *13*, 754−793.

(7) Sajid, M.; Zhao, X.; Liu, D. Production of 2,5-Furandicarboxylic Acid (FDCA) from 5-Hydroxymethylfurfural (HMF): Recent Progress Focusing on the Chemical-Catalytic Routes. *Green Chem.* **2018**, *20*, 5427−5453.

(8) Zhang, Z.; Deng, K. Recent Advances in the Catalytic Synthesis of 2,5-Furandicarboxylic Acid and Its Derivatives. *ACS Catal.* **2015**, *5*, 6529−6544.

(9) Han, X.; Geng, L.; Guo, Y.; Jia, R.; Liu, X.; Zhang, Y.; Wang, Y. Base-free Aerobic Oxidation of 5-Hydroxymethylfurfural to 2,5-Furandicarboxylic Acid over a Pt/C-O-Mg Catalyst. *Green Chem.* **2016**, *18*, 1597−1604.

(10) Wan, X.; Zhou, C.; Chen, J.; Deng, W.; Zhang, Q.; Yang, Y.; Wang, Y. Base-free Aerobic Oxidation of 5-Hydroxymethyl-furfural to 2,5-Furandicarboxylic Acid in Water Catalyzed by Functionalized Carbon Nanotube-Supported Au–Pd Alloy Nanoparticles. *ACS Catal.* **2014**, *4*, 2175−2185.

(11) Yu, K.; Liu, Y.; Lei, D.; Jiang, Y.; Wang, Y.; Feng, Y.; Lou, L.-L.; Liu, S.X.; Zhou, W.Z. $M^{3+}O(-Mn^{4+})_2$ Clusters in Doped MnO_x Catalysts as Promoted Active Sites for the Aerobic Oxidation of 5-Hydroxymethylfurfural. *Catal. Sci. Technol.* **2018**, *8*, 2299−2303.

(12) Hayashi, E.; Yamaguchi, Y.; Kamata, K.; Tsunoda, N.; Kumagai, Y.; Oba, F.; Hara, M. Effect of MnO_2 Crystal Structure on Aerobic Oxidation of 5-Hydroxymethylfurfural to 2,5-Furandicarboxylic Acid. *J. Am. Chem. Soc.* **2019**, *141*, 890−900.

(13) Xu, S.; Zhou, P.; Zhang, Z.; Yang, C.; Zhang, B.; Deng, K.; Bottle, S.; Zhu, H. Selective Oxidation of 5-Hydroxymethylfurfural to 2,5-Furandicarboxylic Acid Using O_2 and a Photocatalyst of Co-thioporphyrazine Bonded to g-C_3N_4. *J. Am. Chem. Soc.* **2017**, *139*, 14775−14782.

(14) Krivtsov, I.; García-López, E. I.; Marcì, G.; Palmisano, L.; Amghouz, Z.; García, J. R.; Ordóñez, S.; Díaz, E. Selective Photocatalytic Oxidation of 5-Hydroxymethyl-2-furfural to 2,5-Furandicarboxyaldehyde in Aqueous Suspension of g-C_3N_4. *Appl. Catal. B: Environ.* **2017**, *204*, 430−439.

(15) Dijkman, W. P.; Groothuis, D. E.; Fraaije, M. W. Enzyme-Catalyzed Oxidation of 5-Hydroxymethylfurfural to Furan-2,5-dicarboxylic Acid. *Angew. Chem. Int. Ed.* **2014**, *53*, 6515−6518.

(16) Sankar, M.; Dimitratos, N.; Miedziak, P. J.; Wells, P. P.; Kiely, C. J.; Hutchings, G. J. Designing Bimetallic Catalysts for a Green and Sustainable Future. *Chem. Soc. Rev.* **2012**, *41*, 8099−8139.

(17) Besson, M.; Gallezot, P.; Pinel, C. Conversion of Biomass into Chemicals over Metal Catalysts. *Chem. Rev.* **2013**, *114*, 1827−1870.

(18) Davis, S. E.; Zope, B. N.; Davis, R. J. On the Mechanism of Selective Oxidation of 5-Hydroxymethylfurfural to 2,5-Furandicarboxylic Acid over Supported Pt and Au Catalysts. *Green Chem.* **2012**, *14*, 143−147.

(19) Ardemani, L.; Cibin, G.; Dent, A. J.; Isaacs, M. A.; Kyriakou, G.; Lee, A. F.; Parlett, C. M. A.; Parry, S. A.; Wilson, K. Solid Base Catalysed 5-HMF Oxidation to 2,5-FDCA over Au/Hydrotalcites: Fact or Fiction? *Chem. Sci.* **2015**, 6, 4940−4945.

(20) Casanova, O.; Iborra, S.; Corma, A. Biomass into Chemicals: Aerobic Oxidation of 5-Hydroxymethyl-2-furfural into 2,5-Furandicarboxylic Acid with Gold Nanoparticle Catalysts. *ChemSusChem* **2009**, *2*, 1138−1144.

(21) Davis, S. E.; Houk, L. R.; Tamargo, E. C.; Datye, A. K.; Davis, R. J. Oxidation of 5-Hydroxymethylfurfural over Supported Pt, Pd and Au Catalysts. *Catal. Today* **2011**, *160*, 55−60.

(22) Zope, B. N.; Hibbitts, D. D.; Neurock, M.; Davis, R. J. Reactivity of the Gold/Water Interface During Selective Oxidation Catalysis. *Science* **2010**, *330*, 74−78.

(23) Gangwal, V. R.; van der Schaaf, J.; Kuster, B. F. M.; Schouten, J. C. Influence of pH on Noble Metal Catalysed Alcohol Oxidation: Reaction Kinetics and Modelling. *J. Catal.* **2005**, *229*, 389−403.

(24) Shen, X.; Liu, W.; Gao, X.; Lu, Z.; Wu, X.; Gao, X. Mechanisms of Oxidase and Superoxide Dismutation-like Activities of Gold, Silver, Platinum, and Palladium, and Their Alloys: A General Way to the Activation of Molecular Oxygen. *J. Am. Chem. Soc.* **2015**, *137*, 15882−15891.

(25) Quon, S.; Jo, D. Y.; Han, G.-H.; Han, S. S.; Seo, M.-G.; Lee, K.-Y. Role of Pt Atoms on Pd(1 1 1) Surface in the Direct Synthesis of Hydrogen Peroxide: Nano-Catalytic Experiments and DFT Calculations. *J. Catal.* **2018**, *368*, 237−247.

(26) Long, R.; Mao, K.; Ye, X.; Yan, W.; Huang, Y.; Wang, J.; Fu, Y.; Wang, X.; Wu, X.; Xie, Y.; Xiong, Y. Surface Facet of Palladium Nanocrystals: A Key Parameter to the Activation of Molecular Oxygen for Organic Catalysis and Cancer Treatment. *J. Am. Chem. Soc.* **2013**, *135*, 3200−3207.

(27) Li, J.; Liu, W.; Wu, X.; Gao, X. Mechanism of pH-Switchable Peroxidase and Catalase-like Activities of Gold, Silver, Platinum and Palladium. *Biomaterials* **2015**, *48*, 37−44.

(28) Yi, G.; Teong, S. P.; Zhang, Y. Base-free Conversion of 5-Hydroxymethylfurfural to 2,5-Furandicarboxylic Acid over a Ru/C Catalyst. *Green Chem.* **2016**, *18*, 979−983.

(29) Lei, D.; Yu, K.; Li, M.-R.; Wang, Y.; Wang, Q.; Liu, T.; Liu, P.; Lou, L.-L.; Wang, G.-C; Liu, S.X. Facet Effect of Single-Crystalline Pd Nanocrystals for Aerobic Oxidation of 5-Hydroxymethyl-2-furfural. *ACS Catal.* **2017**, *7*, 421−432.

(30) Song, H.; Kim, F.; Connor, S.; Somorjai, G. A.; Yang, P. Pt Nanocrystals: Shape Control and Langmuir−Blodgett Monolayer Formation. *J. Phys. Chem. B* **2005**, *109*, 188−193.

(31) Kresse, G.; Hafner, J. *Ab Initio* Molecular-Dynamics Simulation of the Liquid-Metal–Amorphous-Semiconductor Transition in Germanium. *Phys. Rev. B* **1994**, *49*, 14251−14269.

(32) Kresse, G.; Furthmüller, J. Efficiency of *Ab-Initio* Total Energy Calculations for Metals and Semiconductors Using a Plane-Wave Basis Set. *Comp. Mater. Sci.* **1996**, *6*, 15−50.

(33) Kresse, G.; Furthmüller, J. Efficient Iterative Schemes for *Ab Initio* Total-Energy Calculations Using a Plane-Wave Basis Set. *Phys. Rev. B* **1996**, *54*, 11169−11186.

(34) Kresse, G.; Joubert, D. From Ultrasoft Pseudopotentials to the Projector Augmented-Wave Method. *Phys. Rev. B* **1999**, *59*, 1758−1775.

(35) Blöchl, P. E. Projector Augmented-Wave Method. *Phys. Rev. B* **1994**, *50*, 17953−17979.

(36) Henkelman, G.; Uberuaga, B. P.; Jónsson, H. A Climbing image Nudged Elastic Band Method for Finding Saddle Points and Minimum Energy Paths. *J. Chem. Phys.* **2000**, *113*, 9901−9904.

(37) Lide, D. R. Handbook of Chemistry and Physics, 77th ed., CRC Press, New York, 1996-1997.

(38) Monkhorst, H. J.; Pack, J. D. Special Points for Brillouin-Zone Integrations. *Phys. Rev. B* **1976**, *13*, 5188−5192.

(39) Kang, Y.; Li, M.; Cai, Y.; Cargnello, M.; Diaz, R. E.; Gordon, T. R.; Wieder, N. L.; Adzic, R. R.; Gorte, R. J.; Stach, E. A.; Murray, C. B. Heterogeneous Catalysts Need not be so "Heterogeneous": Monodisperse Pt Nanocrystals by Combining Shape-Controlled Synthesis and Purification by Colloidal Recrystallization. *J. Am. Chem. Soc.* **2013**, *135*, 2741−2747.

(40) Arulmozhi, N.; Esau, D.; Lamsal, R. P.; Beauchemin, D.; Jerkiewicz, G. Structural Transformation of Monocrystalline Platinum Electrodes upon Electro-Oxidation and Electro-Dissolution. *ACS Catal.* **2018**, *8*, 6426−6439.

(41) Zhang, Z.; Zhen, J.; Liu, B.; Lv, K.; Deng, K. Selective Aerobic Oxidation of the Biomass-Derived Precursor 5-Hydroxymethylfurfural to 2,5-Furandicarboxylic Acid under Mild Conditions over a Magnetic Palladium Nanocatalysts. *Green Chem.* **2015**, *17*, 1308−1317.

(42) Grass, M. E.; Yue, Y.; Habas, S. E.; Rioux, R. M.; Teall, C. I.; Yang, P.; Somorjai, G. A. Silver Ion Mediated Shape Control of Platinum Nanoparticles: Removal of Silver by Selective Etching Leads to Increased Catalytic Activity. *J. Phys. Chem. C* **2008**, *112*, 4797−4804.

(43) Yu, K.; Lei, D.; Feng, Y.; Yu, H.; Chang, Y.; Wang, Y.; Liu, Y.; Wang, G.-C.; Lou, L.-L.; Liu, S.X.; Zhou, W.Z. The Role of Bi-Doping in Promoting Electron Transfer and Catalytic Performance of Pt/3DOM-$Ce_{1-x}Bi_xO_{2-\delta}$. *J. Catal.* **2018**, *365*, 292−302.

(44) Chen, C.; Li, X.; Wang, L.; Liang, T.; Wang, L.; Zhang, Y.; Zhang, J. Highly Porous Nitrogen- and Phosphorus-Codoped Graphene: An Outstanding Support for Pd Catalysts to Oxidize 5-Hydroxymethylfurfural into 2,5-Furandicarboxylic Acid. *ACS Sustain. Chem. Eng.* **2017**, *5*, 11300−11306.

(45) Li, Q.; Wang, H.; Tian, Z.; Weng, Y.; Wang, C.; Ma, J.; Zhu, C.; Li, W.; Liu, Q.; Ma, L. Selective Oxidation of 5-Hydroxymethylfurfural to 2,5-Furandicarboxylic Acid over Au/CeO_2 Catalysts: The Morphology Effect of CeO_2. *Catal. Sci. Technol*. **2019**, *9*, 1570−1580.

(46) Gupta, K.; Rai, R.K.; Dwivedi, A.D.; Singh, S.K. Catalytic Aerial Oxidation of Biomass-Derived Furans to Furan Carboxylic Acids in Water over Bimetallic Nickel–Palladium Alloy Nanoparticles. *ChemCatChem*, **2017**, *9*, 2760–2767.

(47) Siankevich, S.; Savoglidis, G.; Fei, Z.; Laurenczy, G.; Alexander, D. T. L.; Yan, N.; Dyson, P. J. A Novel Platinum Nanocatalyst for the Oxidation of 5-Hydroxymethylfurfural into 2,5-Furandicarboxylic Acid under Mild Conditions. *J. Catal.* **2014**, *315*, 67−74.

(48) Ait Rass, H.; Essayem, N.; Besson, M. Selective Aerobic Oxidation of 5-HMF into 2,5-Furandicarboxylic Acid with Pt Catalysts Supported on TiO_2- and ZrO_2-Based Supports. *ChemSusChem* **2015**, *8*, 1206−1217.

(49) Wang, G.-C.; Tao, S.-X.; Bu, X.-H. A Systematic Theoretical study of Water Dissociation on Clean and Oxygen-Preadsorbed Transition Metals. *J. Catal.* **2006**, *244*, 10−16.

(50) Xing, B.; Wang, G.-C. Insight into the General Rule for the Activation of the X–H Bonds (X = C, N, O, S) Induced by Chemisorbed Oxygen Atoms. *Phys. Chem. Chem. Phys.* **2014**, *16*, 2621−2629.

(51) Hibbitts, D.; Neurock, M. Promotional Effects of Chemisorbed Oxygen and Hydroxide in the Activation of C–H and O–H Bonds over Transition Metal Surfaces. *Surf. Sci.* **2016**, *650*, 210−220.

The active oxygen species promoted catalytic oxidation of 5-hydroxymethyl-2-furfural on facet-specific Pt nanocrystals

Yaqi Liu, Hong-Yan Ma, Da Lei, Lan-Lan Lou, Shuangxi Liu, Wuzong Zhou, Gui-Chang Wang*, Kai Yu*

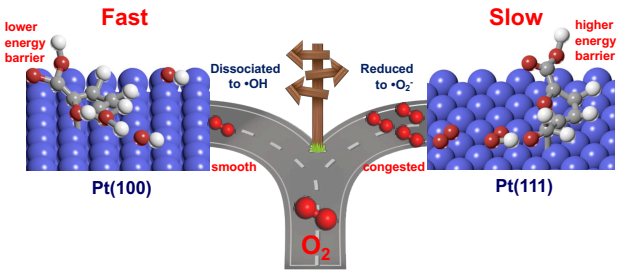

Dehydrogenation of HMFCA with the assistance of active oxygen species